



# Europium-Doped Ceria Nanowires as Anode for Solid Oxide Fuel Cells

Shuai Li<sup>1,2,3\*</sup>, Xia Lu<sup>4</sup>, Siqi Shi<sup>5</sup>, Liqun Chen<sup>3</sup>, Zhaoxiang Wang<sup>3\*</sup> and Yusheng Zhao<sup>1,2\*</sup>

<sup>1</sup> Department of Physics, Academy for Advanced Interdisciplinary Studies, Southern University of Science and Technology, Shenzhen, China, <sup>2</sup> Shenzhen Key Laboratory of Solid State Batteries, Guangdong Provincial Key Laboratory of Energy Materials for Electric Power, Southern University of Science and Technology, Shenzhen, China, <sup>3</sup> Key Laboratory for Renewable Energy, Beijing Key Laboratory for New Energy Materials and Devices, Institute of Physics, Chinese Academy of Sciences, Beijing, China, <sup>4</sup> School of Materials, Sun Yat-sen University, Guangzhou, China, <sup>5</sup> School of Materials Science and Engineering, Shanghai University, Shanghai, China

## OPEN ACCESS

### Edited by:

Asif Mahmood,  
University of Sydney, Australia

### Reviewed by:

Kangning Zhao,  
Shanghai University, China  
Aniruddha Pramod Kulkarni,  
Commonwealth Scientific and  
Industrial Research Organisation  
(CSIRO), Australia

### \*Correspondence:

Shuai Li  
lis6@sustech.edu.cn  
Zhaoxiang Wang  
zxwang@iphy.ac.cn  
Yusheng Zhao  
zhaos@sustech.edu.cn

### Specialty section:

This article was submitted to  
Electrochemistry,  
a section of the journal  
Frontiers in Chemistry

Received: 15 January 2020

Accepted: 03 April 2020

Published: 25 May 2020

### Citation:

Li S, Lu X, Shi S, Chen L, Wang Z and  
Zhao Y (2020) Europium-Doped Ceria  
Nanowires as Anode for Solid Oxide  
Fuel Cells. *Front. Chem.* 8:348.  
doi: 10.3389/fchem.2020.00348

CeO<sub>2</sub>-based materials have been studied intensively as anodes for intermediate temperature solid oxide fuel cells (IT-SOFCs). In this work, pristine and europium (Eu)-doped CeO<sub>2</sub> nanowires were comprehensively investigated as anode materials for IT-SOFCs, by a combination of theoretical predictions and experimental characterizations. The results demonstrate: (1) Oxygen vacancies can be energetically favorably introduced into the CeO<sub>2</sub> lattice by Eu doping; (2) The lattice parameter of the ceria increases linearly with the Eu content when it varies from 0 to 35 mol.%, simultaneously resulting in a significant increase in oxygen vacancies. The concentration of oxygen vacancies reaches its maximum at a ca. 10 mol.% Eu doping level and decreases thereafter; (3) The highest oxygen ion conductivity is achieved at a Eu content of 15 mol.%; while the 10 mol.% Eu-doped CeO<sub>2</sub> sample displays the highest catalytic activity for H<sub>2</sub>-TPR and CO oxidization reactions. The conducting and catalytic properties benefit from the expanded lattice, the large amount of oxygen vacancies, the enhanced reactivity of surface oxygen and the promoted mobility of bulk oxygen ions. These results provide an avenue toward designing and optimizing CeO<sub>2</sub> as a promising anode for SOFCs.

**Keywords:** europium-doped ceria, oxygen vacancy, conductivity, anode, SOFC

## RESEARCH HIGHLIGHTS

- Europium-doped ceria nanowires were synthesized; a maximum 35 mol.% Eu doping into the fluorite CeO<sub>2</sub> lattice can be experimentally achieved.
- The oxygen vacancies were indicated by theoretical calculations, and quantitatively determined by Raman spectroscopy of the Eu-doped CeO<sub>2</sub> samples.
- The 10 mol.% Eu-doped CeO<sub>2</sub> has the highest content of oxygen vacancies, while the 15 mol.% Eu-doped CeO<sub>2</sub> has the highest oxygen ion mobility.
- The 10 mol.% Eu-doped CeO<sub>2</sub> sample was demonstrated to have the best catalytic activity for H<sub>2</sub>-TPR and CO conversion reactions.

## INTRODUCTION

Solid oxide fuel cells (SOFCs) are a kind of high-efficiency and environmental-friendly energy conversion device (Steele and Heinzel, 2001; Brandon et al., 2003; Ormerod, 2003; Choudhury et al., 2013). However, traditional SOFCs based on yttrium stabilized zirconium (YSZ) electrolytes have to work above 800°C due to the low conductivity of the electrolytes and the low catalytic activity of the electrodes (Jacobson, 2010; Coduri et al., 2018; Sreedhar et al., 2019). At such high temperatures, many materials are not stable. Therefore, it is essential to develop SOFC materials with higher conductivity and/or catalytic activity at lower working temperatures (Hibino et al., 2000; Brett et al., 2008; Wachsmann and Lee, 2011). Recently, ceria related materials have been widely studied as electrode materials for intermediate temperature SOFCs (IT-SOFCs) for their unique conduction and catalytic properties at around 500–800°C (Marina et al., 1999; Murray et al., 1999; Goodenough, 2003; Al-Musa et al., 2015; Fan et al., 2017).

SOFCs require anodes that have high ionic ( $O^{2-}$ ) and electronic conductivities for quick charge transfer at the triple-phase-boundary (TPB) and a high catalytic activity for fuel gas oxidation (Jiang and Chan, 2004). Pristine  $CeO_2$  has a fluorite structure in the space group  $Fm-3m$ . Although fast oxygen ion migration is limited in a perfect  $CeO_2$  lattice due to a lack of intrinsic oxygen vacancies,  $CeO_2$  can be tuned to be an  $O^{2-}$  conductor or ion-electron mixed conductor by elemental doping (Mogensen et al., 2000; Skorodumova et al., 2002). On one hand, doping trivalent cations in  $CeO_2$  is an effective way to introduce oxygen vacancies into the lattice, and hence increases the oxygen ionic conductivity (Kim and Ann, 1989; Omar et al., 2007). Anderson et al. suggested that, in order to elevate the ionic conductivity of  $CeO_2$ , the ideal effective atomic number of the dopant should be between 61 and 62 (Andersson et al., 2006).  $Sm^{3+}$  ( $Z = 62$ ) and  $Gd^{3+}$  ( $Z = 63$ ) doped  $CeO_2$  materials (SDC and GDC) were reported to demonstrate the highest oxygen ionic conductivity at  $\sim 1.5 \times 10^{-2} \text{ S cm}^{-1}$  at 700°C (Mogensen et al., 2000; Steele, 2000; Omar et al., 2007). On the other hand, electronic conductivity was also observed for  $CeO_2$  in a reductive atmosphere and/or at high temperatures (Mogensen et al., 2000). Doping mixed-valence elements into  $CeO_2$  can enhance both the ionic and electronic conductivities (Mogensen et al., 2000; Baral and Sankaranarayanan, 2010). Furthermore, the repeatability of  $Ce^{4+}/Ce^{3+}$  redox cycling and the remarkable oxygen storage capability of ceria enhance the catalytic activity of ceria (Sharma et al., 2000), which can be enhanced further by structural manipulation and morphology modification. For example, Pr and Sn doping enhances the catalytic activity of  $CeO_2$  for  $H_2$  or CO oxidization (Xiao et al., 2009; Xian et al., 2013). Reduction of particle size has also been proved effective in improving the catalytic activity of the anode by shortening the ionic diffusion distance and increasing the contacting specific surface area, as is the case in peony-like  $CeO_2$ , which was reported to have a high specific surface area and superior catalytic activity was achieved by doping or surface modification (Sun et al., 2006; Xian et al., 2011).

Europium (Eu,  $Z = 63$ ) is a rare earth element between Sm and Gd. The radius of  $Eu^{3+}$  (1.07Å) is slightly larger than that of  $Ce^{4+}$  (0.97Å). Therefore, Eu could be a promising dopant for  $CeO_2$  when aiming to achieve high ionic conductivity with subtle lattice distortions. Shuk et al. reported that  $Ce_{0.85}Eu_{0.15}O_{1.925-\delta}$  has a conductivity of around  $2.6 \times 10^{-2} \text{ S cm}^{-1}$  with predominantly oxide-ion mobility in air (Shuk et al., 2000). While Baral et al. reported that the total activation energies of  $Ce_{0.80}Eu_{0.20}O_{1.19-\delta}$  were 1.13 and 0.91 eV below and above 470°C, respectively, plausibly indicating different conducting mechanisms in different temperature ranges (Baral and Sankaranarayanan, 2010). On the basis of theoretical calculations, it was shown that the formation energy of oxygen vacancies varies regularly with the atomic number of the dopant in  $CeO_2$  (Andersson et al., 2006; Tang et al., 2010), except for the Eu-doped structure as discussed later. In addition, europium always demonstrates a mixed valence ( $Eu^{2+}/Eu^{3+}$ ) nature. As a result, Eu-doping in  $CeO_2$  is expected to improve both the ionic and electronic conductivities and enhance the catalytic performance accordingly. This suggests an important implication that the conduction and catalytic mechanisms of Eu-doped  $CeO_2$  are influenced by oxygen vacancies, which needs further investigation.

In this work,  $Ce_{1-x}Eu_xO_{2-\delta}$  ( $0 \leq x \leq 0.40$ ; EDC) nanowires were prepared via a co-precipitation method. X-ray diffraction and Raman spectroscopy were employed to characterize the structural properties and oxygen vacancy formation of the as-prepared EDC samples. The dependence of conductivity on Eu doping content was tested by alternating current electrochemical impedance spectroscopy (AC-EIS). The catalytic activity of EDC was evaluated in  $H_2$ -TPR and CO oxidation reactions. The formation of oxygen vacancies and their influence on the conducting and catalytic performances were revealed as follows.

## EXPERIMENTAL SECTION

### Synthesis

EDC nanoparticles were synthesized via a co-precipitation reaction using  $NH_4HCO_3$  as the precipitant. Commercial  $Ce(NO_3)_3 \cdot 6H_2O$  (99%) and  $Eu(NO_3)_3 \cdot 6H_2O$  (99%) were dissolved in de-ionized water homogeneously and then the solution was slowly dropped into an  $NH_4HCO_3$  aqueous solution. The molar concentrations of the metal ions and the precipitant were 0.15 and 0.5 M, respectively, and the molar ratio of all metal ions and  $NH_4^{4+}$  was 1:10 during this process. The mixture was continuously stirred at 80°C for 1 h and then filtered. The precipitate was repeatedly washed using de-ionized water and ethanol, and then dried at 80°C. The precursor was ground and then calcinated in air at 700°C for 5 h. The obtained light yellow powders (and pellets thereof) were referred to as  $CeO_2$ , EDC5, EDC10, EDC15, EDC20, EDC25, EDC30, EDC35, and EDC40, corresponding to the Eu molar ratio of 0, 5, 10, 15%, etc., respectively.  $Ce_{0.8}Sm_{0.2}O_{2-\delta}$  (SDC20) and  $Ce_{0.9}Gd_{0.1}O_{2-\delta}$  (GDC10) samples were also synthesized by the same procedure for comparison.

## Characterizations

The composition of the samples was determined using the inductively coupled plasma Atomic Emission Spectroscopic method (Thermo Electron Corporation). The morphology of the samples was characterized using a scanning electron microscope (SEM, Hitachi S4800). The structure of the powders was analyzed on an X-ray diffractometer (X'Pert Pro MPD) using Cu-K $\alpha$  radiation ( $\lambda \sim 1.54053 \text{ \AA}$ ) and a JY HR800 Raman spectrometer (514 nm radiation and  $2 \text{ cm}^{-1}$  resolution). The XRD refinement was performed with FullProf software. The specific surface areas were measured by the multi-point BET method.

Each EDC powder was combined with a polyvinyl butyral binder and pressed into  $\phi 10 \times 1 \text{ mm}$  pellets and sintered at  $1,350^\circ\text{C}$  for 10 h in air. After cooling down naturally, both sides of the pellets were polished smooth using  $\text{Al}_2\text{O}_3$  paper. Silver paste was brushed uniformly on both sides of the pellet and then heated at  $750^\circ\text{C}$  for 0.5 h. Then EIS measurement was carried out on an IM6e electrochemical station in air (10 mV perturbation voltage and between 3 MHz and 100 mHz) and recorded as a function of temperature from 200 to  $550^\circ\text{C}$ . The reaction activity of the samples with  $\text{H}_2$  was measured on a temperature programmed desorption/reduction (TPD/TPR) instrument (TP-5,080). The EDC nanowires were pelletized to  $-40 \sim +60 \text{ M}$ , preheated in  $\text{N}_2$  at  $400^\circ\text{C}$  for 5 min and cooled down to room temperature, then heated to  $900^\circ\text{C}$  at a rate of  $10^\circ\text{C min}^{-1}$  in flowing  $\text{N}_2$  (*ca.*  $30 \text{ ml min}^{-1}$ ) containing 3 vol.%  $\text{H}_2$  for testing.

The catalytic activity of CO oxidation was tested under atmospheric pressure in a quartz tube reactor. Typically, 50 mg of catalyst was set in the middle of the quartz reactor using quartz wool. A continuous feed with a constant  $\text{CO}/\text{O}_2/\text{N}_2$  at a volume ratio of 2:3:95 was used in this experiment. The effluent gas was analyzed using an on-line gas chromatograph (7890a Agilent) equipped with Porapak Q, ShiCarbon ST and a thermal conductivity detector. The test temperature was varied between 55 and  $300^\circ\text{C}$ , and measured at every  $15^\circ\text{C}$  interval. The conversion of CO was determined as  $\chi_{\text{CO}} = [\text{CO}_2]_{\text{out}} / ([\text{CO}]_{\text{out}} + [\text{CO}_2]_{\text{out}})$ .

## Theoretical Calculations

All total energy density functional theory (DFT) calculations were performed using the Vienna *ab initio* simulation package (VASP) in the framework of the projector augmented wave method. The Perdew-Burke-Ernzerhof functional was taken to deal with the exchange correlation potential. In order to account for the strong on-site Coulomb repulsion among the Ce 4f electrons, a Hubbard parameter  $U$  was added to the DFT functional (DFT+ $U$ ,  $U = 4.5 \text{ eV}$ ). The details for the first-principle simulations are given in a previous work (Yang et al., 2006). The oxygen vacancy formation energy ( $E_{\text{vac}}$ ) was roughly estimated by:  $E_{\text{vac}} = E(\text{cell}_{\text{vac}}) + \frac{1}{2} E(\text{O}_2) - E(\text{cell})$ , where  $E(\text{cell}_{\text{vac}})$  and  $E(\text{cell})$  are the total energies of the optimized supercells with and without an oxygen vacancy, respectively, and  $E(\text{O}_2)$  is the total energy for the ground state of an optimized oxygen molecule in the gas phase. Note that, during the process of the oxygen vacancy formation, the released oxygen atom is expected to form an oxygen molecule.

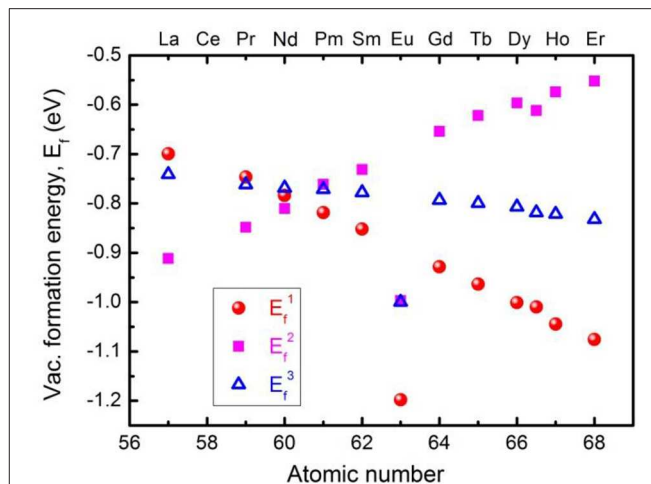


**FIGURE 1** | Formation energies of oxygen vacancy in low content ( $\sim 3.1\%$ )  $M$ -doped  $\text{CeO}_2$  ( $M = \text{La, Pr, Nd, Pm, Sm, Eu, Gd, Tb, Dy, Ho, Er}$ ). The notations of  $E_f^1$ ,  $E_f^2$ , and  $E_f^3$  indicate that the oxygen vacancies are the first, second, and third nearest neighbors to the dopant ions, respectively.

## RESULTS AND DISCUSSION

Before the experimental synthesis and characterization of pristine and Eu-doped  $\text{CeO}_2$  samples, first-principle DFT simulations were performed to explore the formation mechanism and formation energy of oxygen vacancies in the fluorite  $\text{CeO}_2$  structure with/without dopants, which could then be used as a good guide for the subsequent experimental investigations. The derived formation energy,  $E_{\text{vac}}$ , for pristine  $\text{CeO}_2$  was estimated to be 3.10 eV (Tang et al., 2010), which is very close to the results of 3.03 eV given by PBE+ $U$  (Yang et al., 2006), or 3.61 eV from LDA+ $U$  calculations (Andersson et al., 2006). When an oxygen vacancy ( $V_{\text{O}}$  in Kröger-Vink notation) is introduced into the  $\text{CeO}_2$  structure, two electrons will be localized at the 4f orbital of the Ce ions due to the strong correlation interaction, thus transforming two adjacent  $\text{Ce}^{4+}$  ions into a  $\text{Ce}^{3+}$  state and resulting in an obvious distortion of the  $\text{CeO}_6$  octahedron due to small-polaron behavior. **Figure 1** demonstrates the formation energies of oxygen vacancies in low content ( $\sim 3.1 \text{ mol.}\%$ )  $M$ -doped  $\text{CeO}_2$  ( $M = \text{La, Pr, Nd, Pm, Sm, Eu, Gd, Tb, Dy, Ho, and Er}$ ) structures. The results demonstrate that the formation energy of oxygen vacancies in  $\text{CeO}_2$  changes remarkably with different  $M$ -dopants (the atomic number ranges from 57 to 68), indicating a modified structure with excellent oxygen storage and transport applications, *viz.* the existence of oxygen vacancies in the  $M$ -doped  $\text{CeO}_2$  structures are more energetically favorable than in the pristine one. This provides insights into the material design and optimization of  $\text{CeO}_2$ -based anodes for SOFCs. More specifically, the Eu-doped  $\text{CeO}_2$  (EDC) structure demonstrates the lowest oxygen vacancy formation energy of all the studied alternatives, as shown in **Figure 1**, which implies a promising route for research.

As well as the theoretical investigation into oxygen vacancy formation energy, Eu-doped  $\text{CeO}_2$  samples were synthesized

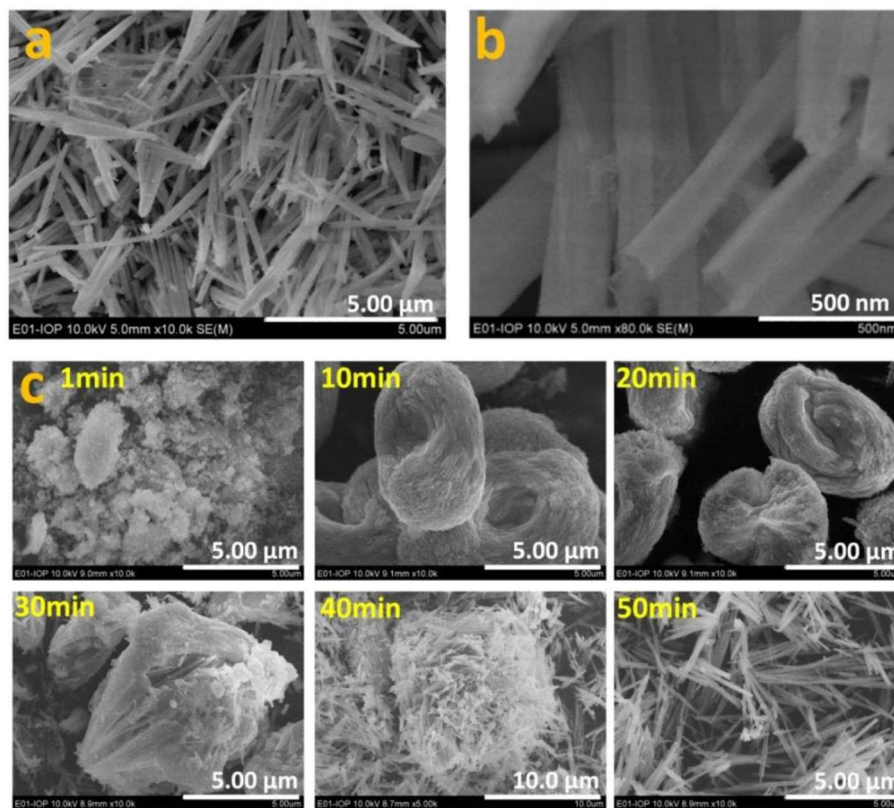


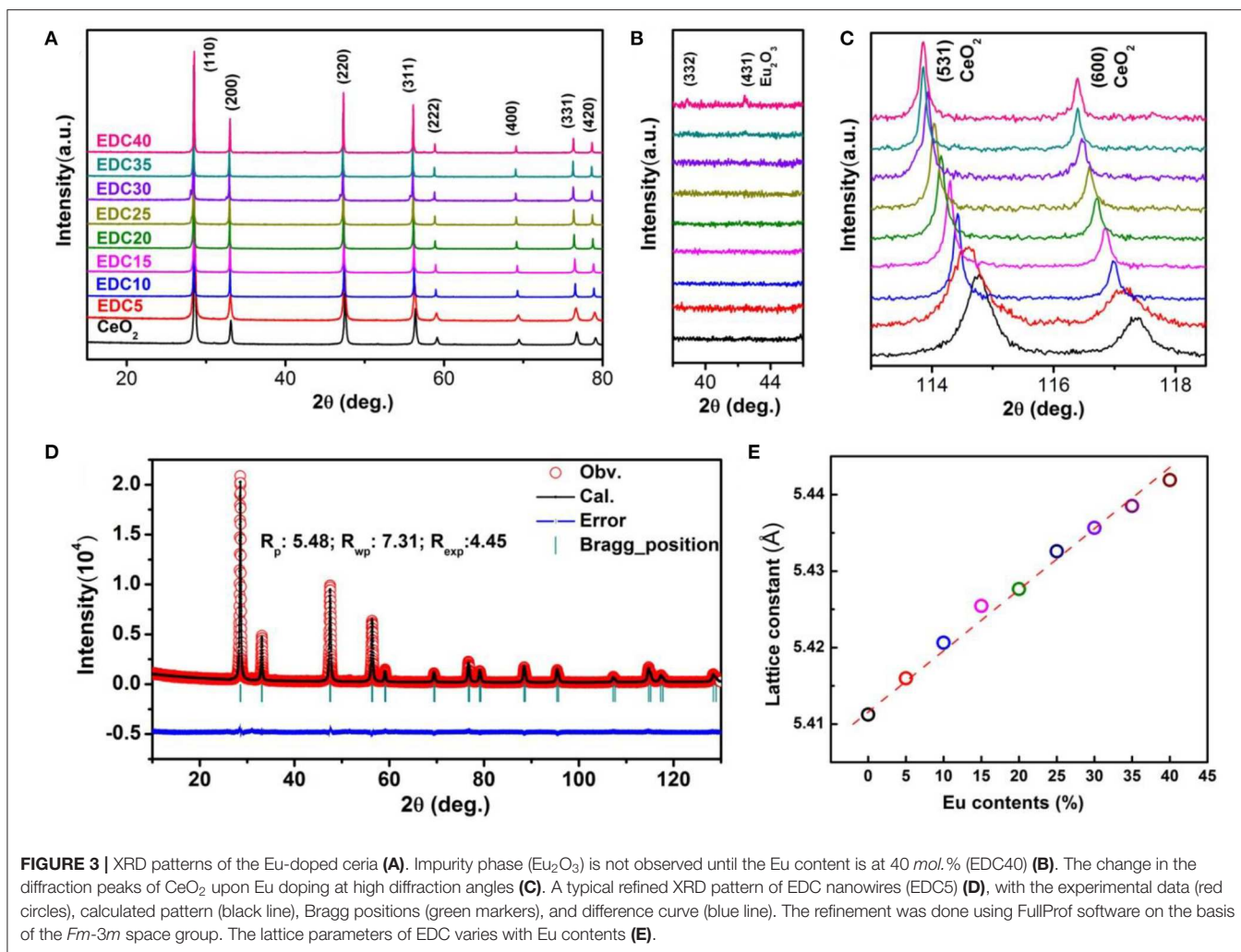
**FIGURE 2** | Morphology of the calcinated EDC5 nanowires (a) and the magnified image (b). The morphology evolution of the precursor with aging time during the co-precipitation process (c).

and characterized systematically. **Figures 2a,b** show that the 5 mol.% Eu-doped  $\text{CeO}_2$  powder is composed of uniform nanowires of 5–10  $\mu\text{m}$  in length and 100 nm in width. The nanowires are actually formed during the co-precipitation process (**Figure 2c**). It is interesting that the co-precipitated precursor is initially nanoparticles and then aggregates into larger nest-like clusters. The nest-like nanostructure is finally disintegrated into nanowires as the aging time increases to ca. 50 min (**Figure 2c**). Calcination at 700°C does not change the morphology of the co-precipitates (**Figure S1**).  $\text{CeO}_2$  nanowires with other Eu doping levels ( $\text{Ce}_{1-x}\text{Eu}_x\text{O}_{2-\delta}$ ;  $0 \leq x \leq 0.20$ ) can be obtained under the same conditions. The width of the EDC nanowires decreases gradually with increasing Eu content. At even higher Eu doping levels ( $0.25 \leq x \leq 0.40$ ), uniform nanoparticles of 10–20 nm are obtained (**Figure S1**). The morphology of the co-precipitation precursor remain unchanged after high temperature calcinated (**Figure S2**). In addition, the specific area of the EDC powders is ca. 30  $\text{m}^2/\text{g}$ , and is roughly independent of the Eu doping content.

The XRD patterns of the as-synthesized EDC samples with different Eu content are shown in **Figure 3**. It can be seen clearly that all the XRD patterns of the EDC samples can be well-indexed into the fluorite structure. The Miller indices of the main peaks have been marked in **Figure 3A**. In addition, the calcinated nanoparticles and the calcinated nanowires show

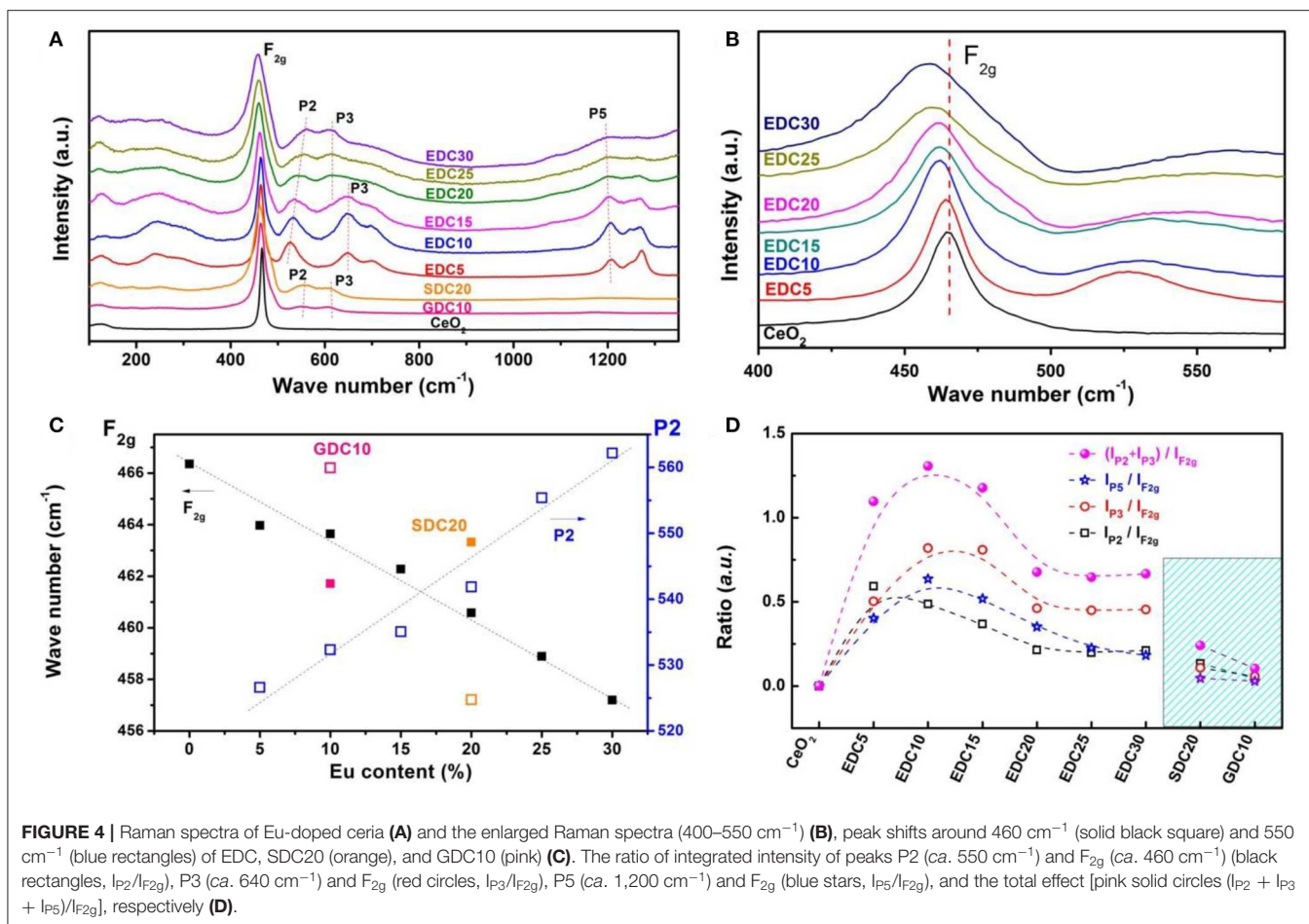
the same XRD patterns as long as their Eu doping content is the same (**Figure S1**). There are no detectable impure phases in the  $\text{CeO}_2$  samples with Eu molar content ranging from 0 to 35%. A diffraction peak for the  $\text{Eu}_2\text{O}_3$  (431) plane is detected in the EDC40 sample as shown in the magnified **Figure 3B**. As the Eu content increases, the main peaks of  $\text{CeO}_2$  shift gradually toward a lower angle, as is shown for the magnified  $\text{CeO}_2$  (531) and (660) diffractions in **Figure 3C**. Particle size of the as-synthesized EDC samples ranges from 10 to 20 nm, calculated by the Scherrer Formula. To obtain the lattice parameters of EDC, refinement was performed using FullProf software. **Figure 3D** shows the typical refinement results of the EDC5 sample. The lattice constant is 5.411 Å for the pristine  $\text{CeO}_2$  and increases linearly with the molar content of Eu, obeying Vegard's rule (Denton and Ashcroft, 1991) (**Figure 3E** and **Table S1**). These results indicate that Eu is successfully doped into  $\text{CeO}_2$  with solid solubility ca. 35 mol.%. As a matter of fact, substitution of larger  $\text{Eu}^{3+}$  ions for smaller  $\text{Ce}^{4+}$  ions in the  $\text{CeO}_2$  lattice results in lattice distortion and the generation of oxygen vacancies for charge balance. Additionally, it is notable that the diffraction peaks narrow gradually as the Eu doping content increases, revealing better crystallinity of the  $\text{CeO}_2$  samples with higher Eu doping levels.

However, the XRD pattern is insensitive to the oxygen vacancies, since they are highly dispersive and of low



concentration. To get further information about the oxygen vacancies, the Raman spectra of EDC samples was collected. The Raman spectrum of SDC and GDC was also collected for comparison (Figure 4A). It can be unambiguously seen that the shape of the spectrum changes gradually with the Eu doping level. In the Raman spectrum of  $\text{CeO}_2$ , there is a strong band located at around  $465\text{ cm}^{-1}$  noted as  $\text{F}_{2g}$ . According to previous reports (Weber et al., 1993; McBride et al., 1994; Pushkarev et al., 2004), this is the only Raman-active mode with triple-degenerated  $\text{F}_{2g}$  symmetry in a perfect  $\text{CeO}_2$  lattice, which can be viewed as a symmetrical breathing mode of the O atoms around the  $\text{Ce}^{4+}$  ions. In our case, the  $\text{F}_{2g}$  mode of pristine  $\text{CeO}_2$  is centered at  $466\text{ cm}^{-1}$ . It gradually shifts to lower frequencies and broadens as the Eu doping amount increases, associating with an asymmetrical trail at the low frequency side and a broad shoulder at the high frequency side (Figures 4A,B). The red-shifts of the  $\text{F}_{2g}$  mode indicate the Ce–O bond changes because of oxygen vacancy formation and lattice dilation as a result of Eu doping. The asymmetrical trail is a result of inhomogeneous strain in the Eu-doped  $\text{CeO}_2$

nanoparticles (Hernandez et al., 2010). In the spectra of doped  $\text{CeO}_2$  samples, a broad shoulder feature appears at around  $550\text{ cm}^{-1}$  (denoted as P2), which has been attributed to the formation of oxygen vacancies by low valence cation doping (Weber et al., 1993; McBride et al., 1994; Pushkarev et al., 2004). The P2 feature, distinct from the  $\text{F}_{2g}$  mode, appears in the spectra of trivalent cation doped  $\text{CeO}_2$  samples (e.g.,  $\text{La}^{3+}$ ,  $\text{Pr}^{3+}$ ,  $\text{Nd}^{3+}$ , etc.), indicating the defect space (involving dopants and oxygen vacancies) deviates from a perfect  $\text{MO}_8$ -type (each cation with 8 nearest O) (McBride et al., 1994; Fu et al., 2003; Dohcevic-Mitrovic et al., 2006). In this work, the P2 feature is prominent when the Eu content is 5 mol.%, and shifts to higher energies as the Eu concentration increases. Figure 4C clearly shows the  $\text{F}_{2g}$  mode (at  $466\text{ cm}^{-1}$  for  $x = 0$  and  $457\text{ cm}^{-1}$  for  $x = 0.30$ ) red-shifts and the P2 mode (at  $526\text{ cm}^{-1}$  for  $x = 0.05$  and  $562\text{ cm}^{-1}$  for  $x = 0.30$ ) blue-shifts in the  $\text{Ce}_{1-x}\text{Eu}_x\text{O}_{2-\delta}$  samples. These features of SDC20 and GDC10 samples are also shown for comparison. These results distinctly confirm that Eu is successfully doped into the  $\text{CeO}_2$  lattice with oxygen vacancies introduced to compensate for the charge, and the

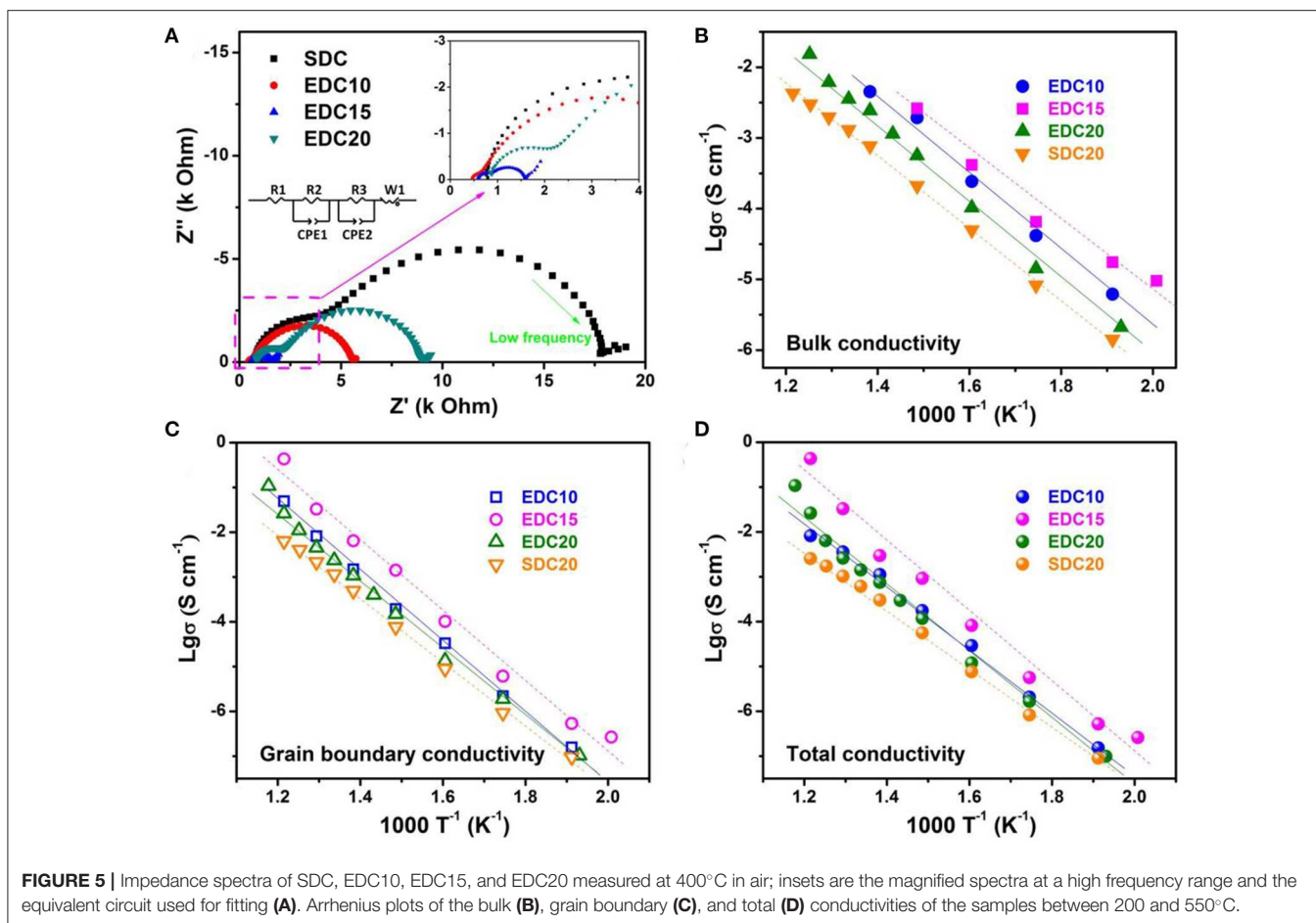


structure distortion is noted as a linear expansion referring to the XRD analyses.

Besides the P2 feature, other peaks also appear in the Raman spectra of doped CeO<sub>2</sub> samples. The peak noted as P3 (ca. 640 cm<sup>-1</sup>) is attributed to the oxygen vacancies related to Ce<sup>3+</sup> in the CeO<sub>2</sub> lattice (Pu et al., 2007). This feature is absent in the Raman spectrum of pristine CeO<sub>2</sub>, suggesting negligible intrinsic oxygen vacancies in the pristine ceria. It emerges with Eu-, Sm-, and Gd-doping, and becomes remarkable for EDC5, EDC10, and EDC15 samples. The peak noted as P5 (ca. 1,200 cm<sup>-1</sup>) is attributed to the O–O vibration in superoxide species, which comes from O<sub>2</sub> adsorption on surface defects or oxygen vacancies in the surface or subsurface of Eu-doped CeO<sub>2</sub> samples. As the P2, P3, and P5 modes are related to oxygen vacancies, and the F<sub>2g</sub> mode indicates the Ce–O breathing mode, the ratio between integrated intensities of the P2, P3, P5 and that of the F<sub>2g</sub> peaks (I<sub>P2</sub>/I<sub>F2g</sub>, I<sub>P3</sub>/I<sub>F2g</sub>, I<sub>P5</sub>/I<sub>F2g</sub> (I<sub>P2</sub> + I<sub>P3</sub> + I<sub>P5</sub>)/I<sub>F2g</sub>) can be used to evaluate the concentration of oxygen vacancies (Mcbride et al., 1994). That is, the higher the ratio, the more oxygen vacancies in the lattice. **Figure 4D** shows the dependence of I<sub>P2</sub>/I<sub>F2g</sub>, I<sub>P3</sub>/I<sub>F2g</sub>, I<sub>P5</sub>/I<sub>F2g</sub>, and (I<sub>P2</sub> + I<sub>P3</sub> + I<sub>P5</sub>)/I<sub>F2g</sub> on the Eu concentration in comparison with those of SDC20 and GDC10. The trend of I<sub>P2</sub>/I<sub>F2g</sub> suggests that substitution of Ce<sup>4+</sup> with

Eu<sup>3+</sup> can greatly enhance the amount of oxygen vacancies even with 5 mol.% Eu content; while this type of oxygen vacancy decreases gradually as the Eu concentration further increases. Meanwhile doping Eu<sup>3+</sup> into CeO<sub>2</sub> also results in the formation of Ce<sup>3+</sup> and oxygen vacancies in the lattice, as indicated by the I<sub>P3</sub>/I<sub>F2g</sub> ratio change, and this type of oxygen vacancy reaches its maximum amount at around the 10–15 mol.% doping level and then decreases gradually. For the surface and subsurface oxygen species, they are enhanced greatly by Eu<sup>3+</sup> doping and reach a maximum around the 10 mol.% doping level as shown by the change in the I<sub>P5</sub>/I<sub>F2g</sub> ratio in **Figure 4D**. In summary, Eu<sup>3+</sup> doping into CeO<sub>2</sub> introduces a large amount of oxygen vacancies in the lattice via charge balancing, and also enhances the surface O<sub>2</sub> adsorption property. A possible reason could be that the ionic radius of Eu<sup>3+</sup> is 1.07 Å, a little bit larger than that of Ce<sup>4+</sup> at 0.97 Å. This makes it easy for Eu to enter into the CeO<sub>2</sub> lattice and introduce many oxygen vacancies with little lattice distortion. Among all Eu-, Sm-, and Gd-doped CeO<sub>2</sub> samples studied here, the optimal doping level is demonstrated to be around 10 mol.% Eu content to achieve the most oxygen vacancies.

Raman spectrum analysis confirms the introduction of oxygen vacancies into the Eu-doped CeO<sub>2</sub> lattice, which is a prerequisite



for better electrochemical performance of EDC as an anode. Furthermore, it is also important to investigate oxygen/vacancy diffusion kinetics. Here, alternating current electrochemical impedance spectroscopy (AC-EIS) was employed to investigate the Eu-content dependent conductivity of EDC10, EDC15, EDC20, and SDC20 samples. The pellets were sintered at 1,350°C for 10 h to get a dense ceramic, in an attempt to diminish the grain boundary resistance (details shown in **Figure S3**). The typical impedance spectra of these samples measured at 400°C in air (**Figure 5A**) consists of two typical semicircles. The semicircles at the higher frequency range (inset of **Figure 5A**) are ascribed to the bulk resistance. The semicircles at the lower frequency range are ascribed to grain boundary resistance. Equivalent circuit (inset of **Figure 5A**) is used to resolve the EIS spectrum. The variation of the calculated conductivities of the bulk, the grain boundary and the total are shown in **Figures 5B–D** and **Table S2**, respectively. They all basically obey the Arrhenius equation in the studied temperature range (200–550°C). The EDC15 sample has higher bulk, grain boundary and total conductivities than any other sample. At 550°C, the total conductivity of the EDC15 sample is  $3.6 \times 10^{-1} \text{ S cm}^{-1}$ , about two orders of magnitude higher than that of the SDC20 sample, one order higher than that of the EDC20 and EDC10 samples.

Derived from the Arrhenius plot, the total conducting activation energy of EDC15 at the measured temperature range is 1.37 eV. Referring to above analysis, the enhanced conductivity probably arises from the higher concentration of oxygen vacancies in EDC15 than in the SDC20 and EDC20 samples. However, it is interesting that although the EDC10 sample has more oxygen vacancies, its conductivity is lower than that of the EDC15 sample. This could be attributed to the competitive effects of oxygen vacancy formation and migration. On one hand, in the EDC10 sample, it is probably easy for the oxygen vacancies to associate with surface/bulk oxygen species (as indicated by  $I_{P5}/I_{F2g}$  in **Figure 4D**). On the other hand, the lattice constant of the EDC15 sample is larger than that of EDC10, favoring  $O^{2-}$  migration.

The morphology, grain size, lattice parameters, and ion migration have a large influence on catalytic properties (Zhao et al., 2018; Lian et al., 2019). Subsequently, improvement of the catalytic properties of the EDC samples was evaluated by  $H_2$ -TPR and CO oxidation reactions. The reducibility of the pristine and EDC samples was examined by  $H_2$ -TPR analysis as shown in **Figure 6**. The peak position and peak area in the  $H_2$ -TPR profiles were determined as shown in **Table 1**. According to a previous report, the low temperature peak (LT, below 600°C) and

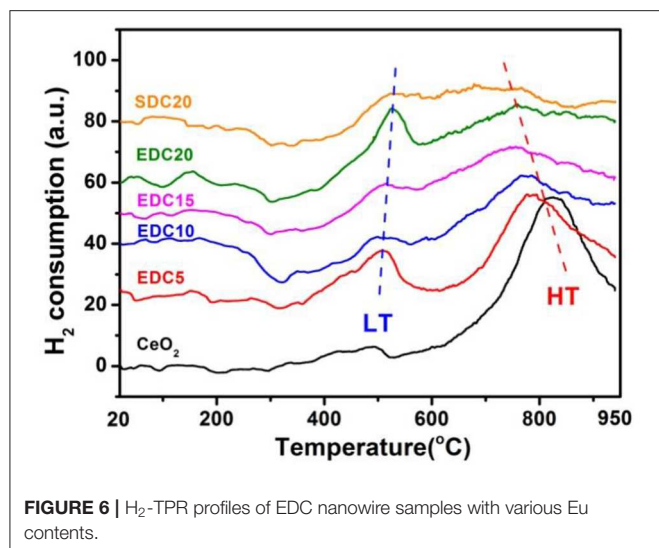


FIGURE 6 | H<sub>2</sub>-TPR profiles of EDC nanowire samples with various Eu contents.

TABLE 1 | H<sub>2</sub>-TPR results for EDC samples.

Sample	Peak position (°C)	Peak area (a.u.)			
		(H <sub>2</sub> consumption)			
		LT	HT	LT	HT
CeO <sub>2</sub>	495	825	0.36	5.15	
EDC5	510	781	1.61	3.68	
EDC10	510	764	0.38	2.3	
EDC15	515	761	0.51	2.22	
EDC20	525	756	1.20	1.55	

the high temperature peak (HT, around 800°C) are ascribed to the reduction of the oxygen species on the surface and in the bulk of CeO<sub>2</sub>, respectively (Hernandez et al., 2010). In this work, the weak LT and strong HT peaks of pristine CeO<sub>2</sub> nanowires are centered at 495 and 825°C, respectively. Doping Eu into CeO<sub>2</sub> introduces abundant oxygen vacancies into the lattice, which changes the oxygen mobility and adsorption properties, and hence affects the reactivity of the LT and HT reduction processes. In more detail, firstly, the LT peak becomes prominent for Eu-doped CeO<sub>2</sub> with more hydrogen consumption indicated by the integrated peak area as shown in Table 1. Secondly, the position of the LT peak shifts slightly to higher temperatures with increasing Eu content as shown in Figure 6. Thirdly, the HT peak shifts to lower temperatures, and the area of this peak becomes smaller, as the Eu content increases as shown in Figure 6 and Table 1. This is indicative of the enhanced oxygen mobility in the bulk with Eu-doping. However, the low reaction activity of surface oxygen and poor oxygen ion diffusion kinetics indicates that there are few oxygen vacancies in the pristine CeO<sub>2</sub> sample, consistent with the Raman results as shown in Figure 4.

The color of the pure CeO<sub>2</sub> sample is pale yellow due to Ce<sup>4+</sup>-O<sup>2-</sup> charge transfer. It turns blue upon reduction (CeO<sub>2-x</sub>), and turns black when CeO<sub>2</sub> becomes grossly non-stoichiometric

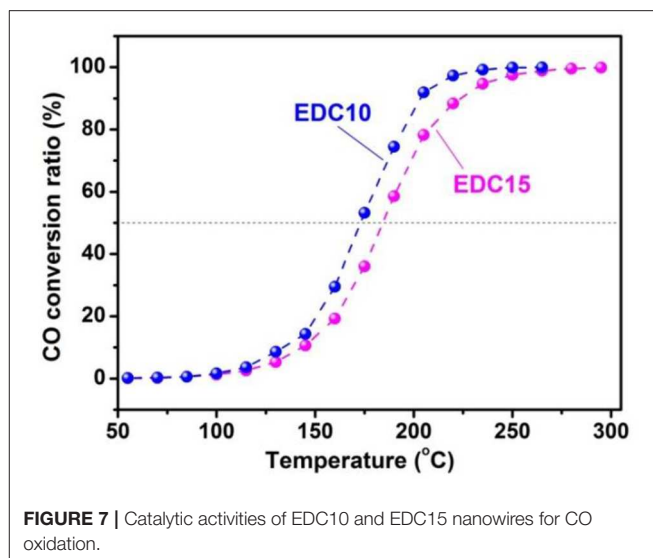


FIGURE 7 | Catalytic activities of EDC10 and EDC15 nanowires for CO oxidation.

(from over reduction) (Mogensen et al., 2000). However, it should be pointed out that in this work the color of CeO<sub>2</sub> (pale yellow) became lighter as more Eu was doped. After H<sub>2</sub>-TPR testing and cooling down to room temperature, the pristine CeO<sub>2</sub> and all of the doped CeO<sub>2</sub> samples in the quartz tube become dark blue, indicating considerable reduction by H<sub>2</sub> and formation of a non-stoichiometric CeO<sub>2-x</sub> state with plenty of oxygen vacancies. However, the color of the reduced EDC10 sample recovered to yellow as soon as it was exposed to air, and even set fire to the weighing paper. Obviously this is an exothermic process, during which the H<sub>2</sub>-reduced sample regains oxygen from the air. The color change of the reduced EDC10 sample is the most prominent and strongest of all, with all of the particles turning back to yellow in a few seconds. For the H<sub>2</sub>-reduced EDC5, EDC15, EDC20, and SDC20 samples, the color change process is much slower and some of the particles remained dark blue in air. This color conversion phenomena implies that the 10 mol.% Eu doped CeO<sub>2</sub> probably has the most stable fluorite structure with respect to other samples, and it also favors O<sup>2-</sup> migration and O<sub>2</sub> adsorption. In addition, nearly all the particles of the reduced CeO<sub>2</sub> remained dark blue after exposure to air for a few days. These results suggest that Eu doping in the lattice significantly enhances the catalytic activity of CeO<sub>2</sub> on H<sub>2</sub>-TPR. The catalytic performance demonstrates a Eu-content dependent relationship. Optimal catalytic activity is obtained when the doping level is 10 mol.% as shown by the H<sub>2</sub>-TPR tests above.

Concerning the real life conditions for use as an anode for SOFCs, the catalytic activity of the EDC10 (highest catalytic activity on H<sub>2</sub>-TPR) and EDC15 (highest conductivity) samples are further examined on CO oxidation reaction. The catalytic curves for EDC10 and EDC15 samples are shown in Figure 7. A CO conversion ratio of 100% is achieved before 300°C, indicating that both the EDC10 and EDC15 samples are promising candidates for anode materials. As predicted with the Raman spectroscopic analysis and H<sub>2</sub>-TPR test, the catalytic activity

of EDC10 is found to be higher than that of EDC15 for CO oxidation. **Figure 7** shows clearly that the  $T_{50}$  (temperature for 50% CO conversion) for EDC10 and EDC15 are 173 and 184°C, respectively, and  $T_{90}$  (temperature for 90% CO conversion) for EDC10 and EDC15 are 204 and 225°C, respectively. These results indicate that EDC10 can work at lower temperatures than EDC15 as an anode material for IT-SOFCs, and the catalytic performance of EDC10 is better accordingly. Since the samples under investigation have similar morphology and specific surface area, the difference in catalytic activity here is taken to arise from the comprehensive effects of oxygen vacancy concentration, oxygen ion mobility and reactivity as discussed above. This also confirms that the optimal content is around 10 mol.% Eu doping in CeO<sub>2</sub> for application as an SOFC anode.

## CONCLUSIONS

Fluorite structure Eu-doped CeO<sub>2</sub> samples, with nanowire morphology, were synthesized via a co-precipitation method. The solid solubility of Eu in CeO<sub>2</sub> structures is *ca.* 35 mol.%. Below the solid solubility, the lattice parameter of ceria increases linearly with the content of Eu, obeying Vegard's law. Doping Eu into CeO<sub>2</sub> introduces a large amount of oxygen vacancies, and hence enhances the conductivity and catalytic activity. Consequently, the EIS results show that EDC15 (15 mol.% Eu-doped CeO<sub>2</sub>) has the highest conductivity among the samples, while the H<sub>2</sub>-TPR and CO oxidation results demonstrate the EDC10 sample (10 mol.% Eu-doped CeO<sub>2</sub>) has the highest catalytic activity. The enhanced conducting and catalytic properties are ascribed to the formation of abundant oxygen vacancies, associated with the enhanced reactivity of surface

oxygen and the mobility of bulk oxygen ions in the expanded lattice. Overall, Eu-doped CeO<sub>2</sub> nanowires, especially the *ca.* 10 mol.% Eu doped sample, exhibit promising application potential as anode materials in IT-SOFCs. All of these findings provide a comprehensive path for material design and optimization for SOFCs.

## AUTHOR CONTRIBUTIONS

SL contributed ideas, designed the work, performed experiments and data analysis, and wrote the manuscript. XL contributed to lattice parameter refinement. SS contributed to the theoretical calculations. LC, ZW, and YZ contributed to discussing this work, editing the manuscript, providing laboratory platform and financial support.

## FUNDING

The authors are grateful for financial support from the Key Program of the National Natural Science Foundation of China (No. 51732005), Guangdong Provincial Key Laboratory of Energy Materials for Electric Power (No. 2018B030322001), Shenzhen Clean Energy Research Institute (No. CERI-KY-2019-003), and Shenzhen Key Laboratory of Solid State Batteries (No. ZDSYS20180208184346531).

## SUPPLEMENTARY MATERIAL

The Supplementary Material for this article can be found online at: <https://www.frontiersin.org/articles/10.3389/fchem.2020.00348/full#supplementary-material>

## REFERENCES

- Al-Musa, A. A., Al-Saleh, M., Al-Zahrani, A., Kaklidis, N., and Marnellos, G. (2015). Electro-catalytic and fuel cell studies in an internal reforming iso-octane fed SOFC using Cu/CeO<sub>2</sub> composites as anodic electrodes. *ECS Trans.* 66, 125–136. doi: 10.1149/06603.0125ecst
- Andersson, D. A., Simak, S. I., Skorodumova, N. V., Abrikosov, I. A., and Johansson, B. (2006). Optimization of ionic conductivity in doped ceria. *Proc. Natl. Acad. Sci. U.S.A.* 103, 3518–3521. doi: 10.1073/pnas.0509537103
- Baral, A. K., and Sankaranarayanan, V. (2010). Ionic transport properties in nanocrystalline Ce<sub>0.8</sub>A<sub>0.2</sub>O<sub>2-δ</sub> (with A = Eu, Gd, Dy, and Ho) materials. *Nanoscale Res. Lett.* 5, 637–643. doi: 10.1007/s11671-010-9527-z
- Brandon, N. P., Skinner, S., and Steele, B. C. H. (2003). Recent advances in materials for fuel cells. *Annu. Rev. Mater. Res.* 33, 183–213. doi: 10.1146/annurev.matsci.33.022802.094122
- Brett, D. J. L., Atkinson, A., Brandon, N. P., and Skinner, S. J. (2008). Intermediate temperature solid oxide fuel cells. *Chem. Soc. Rev.* 37, 1568–1578. doi: 10.1039/b612060c
- Choudhury, A., Chandra, H., and Arora, A. (2013). Application of solid oxide fuel cell technology for power generation—a review. *Renew. Sustain. Energy Rev.* 20, 430–442. doi: 10.1016/j.rser.2012.11.031
- Coduri, M., Checchia, S., Longhi, M., Ceresoli, D., and Scavini, M. (2018). Rare earth doped ceria: the complex connection between structure and properties. *Front. Chem.* 6:526. doi: 10.3389/fchem.2018.00526
- Denton, A. R., and Ashcroft, N. W. (1991). Vegard law. *Phys. Rev. A.* 43, 3161–3164. doi: 10.1103/PhysRevA.43.3161
- Dohcevic-Mitrovic, Z. D., Scepanovic, M. J., Grujic-Brojcin, M. U., Popovic, Z. V., Boskovic, S. B., Matovic, B. M., et al. (2006). The size and strain effects on the Raman spectra of Ce<sub>1-x</sub>Nd<sub>x</sub>O<sub>2-δ</sub> (0 ≤ x ≤ 0.25) nanopowders. *Solid State Commun.* 137, 387–390. doi: 10.1016/j.ssc.2005.12.006
- Fan, L. D., He, C. X., and Zhu, B. (2017). Role of carbonate phase in ceria-carbonate composite for low temperature solid oxide fuel cells: a review. *Int. J. Energy Res.* 25, 465–481. doi: 10.1002/er.3629
- Fu, Q., Saltsburg, H., and Flytzani-Stephanopoulos, M. (2003). Active nonmetallic Au and Pt species on ceria-based water-gas shift catalysts. *Science* 301, 935–938. doi: 10.1126/science.1085721
- Goodenough, J. B. (2003). Oxide-ion electrolytes. *Annu. Rev. Mater. Res.* 33, 91–128. doi: 10.1146/annurev.matsci.33.022802.091651
- Hernandez, W. Y., Romero-Sarria, F., Centeno, M. A., and Odriozola, J. A. (2010). *In situ* characterization of the dynamic gold-support interaction over ceria modified Eu<sup>3+</sup>. Influence of the oxygen vacancies on the CO oxidation reaction. *J. Phys. Chem. C* 114, 10857–10865. doi: 10.1021/jp1013225
- Hibino, T., Hashimoto, A., Inoue, T., Tokuno, J., Yoshida, S., and Sano, M. (2000). A low-operating-temperature solid oxide fuel cell in hydrocarbon-air mixtures. *Science* 288, 2031–2033. doi: 10.1126/science.288.5473.2031
- Jacobson, A. J. (2010). Materials for solid oxide fuel cells. *Chem. Mater.* 22, 660–674. doi: 10.1021/cm902640j
- Jiang, S. P., and Chan, S. H. (2004). A review of anode materials development in solid oxide fuel cells. *J. Mater. Sci.* 39, 4405–4439. doi: 10.1023/B:JMASC.0000034135.52164.6b
- Kim, D. J., and Ann, A. (1989). Lattice parameters, ionic conductivities, and solubility limits in fluorite-structure MO<sub>2</sub> oxide (M = Hf<sup>4+</sup>, Zr<sup>4+</sup>,

- Ce<sup>4+</sup>, Th<sup>4+</sup>, V<sup>4+</sup>) solid-solutions. *J. Am. Ceramic Soc.* 72, 1415–1421. doi: 10.1111/j.1151-2916.1989.tb07663.x
- Lian, S. T., Sun, C. L., Xu, W. N., Luo, W. C., Zhao, K. N., Yao, G., et al. (2019). Built-in oriented electric field facilitating durable ZnMnO<sub>2</sub> battery. *Nano Energy* 62, 79–84. doi: 10.1016/j.nanoen.2019.04.038
- Marina, O. A., Bagger, C., Primdahl, S., and Mogensen, M. (1999). A solid oxide fuel cell with a gadolinia-doped ceria anode: preparation and performance. *Solid State Ionics* 123, 199–208. doi: 10.1016/S0167-2738(99)00111-3
- McBride, J. R., Hass, K. C., Poindexter, B. D., and Weber, W. H. (1994). Raman and X-ray studies of Ce<sub>1-x</sub>Re<sub>x</sub>O<sub>2-y</sub>, where Re=La, Pr, Nd, Eu, Gd, and Tb. *J. Appl. Phys.* 76, 2435–2441. doi: 10.1063/1.357593
- Mogensen, M., Sammes, N. M., and Tompsett, G. A. (2000). Physical, chemical and electrochemical properties of pure and doped ceria. *Solid State Ionics* 129, 63–94. doi: 10.1016/S0167-2738(99)00318-5
- Murray, E. P., Tsai, T., and Barnett, S. A. (1999). A direct-methane fuel cell with a ceria-based anode. *Nature* 400, 649–651. doi: 10.1038/23220
- Omar, S., Wachsman, E. D., and Nino, J. C. (2007). Higher ionic conductive ceria-based electrolytes for solid oxide fuel cells. *Appl. Phys. Lett.* 91:144106. doi: 10.1063/1.2794725
- Ormerod, R. M. (2003). Solid oxide fuel cells. *Chem. Soc. Rev.* 32, 17–28. doi: 10.1039/b105764m
- Pu, Z. Y., Lu, J. Q., Luo, M. F., and Me, Y. L. (2007). Study of oxygen vacancies in Ce<sub>0.9</sub>Pr<sub>0.1</sub>O<sub>2-δ</sub> solid solution by *in situ* x-ray diffraction and *in situ* Raman spectroscopy. *J. Phys. Chem. C* 111, 18695–18702. doi: 10.1021/jp0759776
- Pushkarev, V. V., Kovalchuk, V. I., and d'Itri, J. L. (2004). Probing defect sites on the CeO<sub>2</sub> surface with dioxygen. *J. Phys. Chem. B* 108, 5341–5348. doi: 10.1021/jp0311254
- Sharma, S., Hilaire, S., Vohs, J. M., Gorte, R. J., and Jen, H. W. (2000). Evidence for oxidation of ceria by CO<sub>2</sub>. *J. Catal.* 190, 199–204. doi: 10.1006/jcat.1999.2746
- Shuk, P., Greenblatt, M., and Croft, M. (2000). Hydrothermal synthesis and properties of Ce<sub>1-x</sub>Eu<sub>x</sub>O<sub>2-δ</sub> solid solutions. *J. Alloys Compounds* 303, 465–471. doi: 10.1016/S0925-8388(00)00627-7
- Skorodumova, N. V., Simak, S. I., Lundqvist, B. I., Abrikosov, I. A., and Johansson, B. (2002). Quantum origin of the oxygen storage capability of ceria. *Phys. Rev. Lett.* 89:166601. doi: 10.1103/PhysRevLett.89.166601
- Sreedhar, I., Agarwal, B., Goyal, P., and Singh, S. A. (2019). Recent advances in material and performance aspects of solid oxide fuel cells. *J. Electroanal. Chem.* 848:113315. doi: 10.1016/j.jelechem.2019.113315
- Steele, B. C. H. (2000). Appraisal of Ce<sub>1-y</sub>Gd<sub>y</sub>O<sub>2-y/2</sub> electrolytes for IT-SOFC operation at 500 °C. *Solid State Ionics* 129, 95–110. doi: 10.1016/S0167-2738(99)00319-7
- Steele, B. C. H., and Heinzl, A. (2001). Materials for fuel-cell technologies. *Nature* 414, 345–352. doi: 10.1038/35104620
- Sun, C. W., Sun, J., Xiao, G. L., Zhang, H. R., Qiu, X. P., Li, H., et al. (2006). Mesoscale organization of nearly monodisperse flowerlike ceria microspheres. *J. Phys. Chem. B* 110, 13445–13452. doi: 10.1021/jp062179r
- Tang, Y. H., Zhang, H., Cui, L. X., Ouyang, C. Y., Shi, S. Q., Tang, W. H., et al. (2010). First-principles investigation on redox properties of M-doped CeO<sub>2</sub> (M = Mn, Pr, Sn, Zr). *Phys. Rev. B* 82:125104. doi: 10.1103/PhysRevB.82.125104
- Wachsman, E. D., and Lee, K. T. (2011). Lowering the temperature of solid oxide fuel cells. *Science* 334, 935–939. doi: 10.1126/science.1204090
- Weber, W., Hass, K., and McBride, J. (1993). Raman study of CeO<sub>2</sub>: second-order scattering, lattice dynamics, and particle-size effects. *Phys. Rev. B* 48, 178–185. doi: 10.1103/PhysRevB.48.178
- Xian, C. N., Li, H., Chen, L. Q., and Lee, J. S. (2011). Morphological and catalytic stability of mesoporous peony-like ceria. *Microporous Mesoporous Mater.* 142, 202–207. doi: 10.1016/j.micromeso.2010.11.037
- Xian, C. N., Wang, S. F., Sun, C. W., Li, H., Chan, S. W., and Chen, L. Q. (2013). Effect of Ni doping on the catalytic properties of nanostructured peony-like CeO<sub>2</sub>. *Chin. J. Catal.* 34, 305–312. doi: 10.1016/S1872-2067(11)60466-X
- Xiao, G. L., Li, S. A., Li, H., and Chen, L. Q. (2009). Synthesis of doped ceria with mesoporous flowerlike morphology and its catalytic performance for CO oxidation. *Microporous Mesoporous Mater.* 120, 426–431. doi: 10.1016/j.micromeso.2008.12.015
- Yang, Z., Woo, T. K., and Hermansson, K. (2006). Effects of Zr doping on stoichiometric and reduced ceria: a first-principles study. 124:224740doi: 10.1063/1.2200354
- Zhao, K. N., Sun, C. L., Yu, Y. H., Dong, Y. F., Zhang, C. Y., Wang, C. M., et al. (2018). Surface gradient Ti-doped MnO<sub>2</sub> nanowires for high-rate and long-life lithium battery. *ACS Appl. Mater. Interfaces* 10, 44376–44384. doi: 10.1021/acsami.8b13376

**Conflict of Interest:** The authors declare that the research was conducted in the absence of any commercial or financial relationships that could be construed as a potential conflict of interest.

The reviewer KZ declared a shared affiliation, though no other collaboration, with one of the authors SS to the handling editor.

Copyright © 2020 Li, Lu, Shi, Chen, Wang and Zhao. This is an open-access article distributed under the terms of the Creative Commons Attribution License (CC BY). The use, distribution or reproduction in other forums is permitted, provided the original author(s) and the copyright owner(s) are credited and that the original publication in this journal is cited, in accordance with accepted academic practice. No use, distribution or reproduction is permitted which does not comply with these terms.